

Dynamical mean field theory for manganites

Y.-F. Yang^{1,2} and K. Held³¹*Los Alamos National Laboratory, Los Alamos, New Mexico 87545, USA*²*Institute of Physics, Chinese Academy of Sciences, Beijing 100190, China*³*Institute of Solid State Physics, Vienna University of Technology, 1040 Vienna, Austria*

(Received 17 March 2009; revised manuscript received 5 May 2010; published 9 November 2010)

Doped and undoped manganites are modeled by the coupling between itinerant e_g electrons and static t_{2g} spins, the Jahn-Teller and breathing phonon modes, and the Coulomb interaction. We provide for a careful estimate of all parameters and solve the corresponding Hamiltonian by dynamical mean field theory. Our results for the one-electron spectrum, the optical conductivity, the dynamic and static lattice distortion, as well as the Curie temperature show the importance of all of the above ingredients for a realistic calculation as well as for describing the unusual dynamical properties of manganites including the insulating parent compound and the insulatinglike paramagnetic state of doped manganites.

DOI: [10.1103/PhysRevB.82.195109](https://doi.org/10.1103/PhysRevB.82.195109)

PACS number(s): 71.27.+a, 71.10.Fd, 75.47.Gk

I. INTRODUCTION

Manganites have attracted intensive interest during the last decades due to their extraordinary properties including the colossal magnetoresistance (CMR).^{1–3} These materials have the chemical composition $T_{1-x}D_x\text{MnO}_3$, where T is a trivalent rare earth ion ($T=\text{La, Pr, Nd, \dots}$) and D is a divalent alkali ion ($D=\text{Ca, Sr, \dots}$) and crystallize in a cubic perovskite structure with a possible distortion at low temperatures, see Fig. 1, which albeit can be distorted at low temperatures. Soon after CMR was discovered, various phase diagrams as a function of temperature and magnetic field or doping concentration x were established,^{4–12} also see the review articles Refs. 13–16. For the parent compound LaMnO_3 , an insulator-to-metal transition was found upon applying pressure;¹⁷ and a charge/orbital-ordered phase has been reported in a large number of perovskite ($T_{1-x}D_x\text{MnO}_3$) and layered ($T_{1-x}D_{1+x}\text{MnO}_4$) manganites, depending on the effective bandwidth and the quenched disorder.^{18,19} The dynamical properties of the paramagnetic insulating are very unusual as is reflected in a spectral function $A(\omega)$ with a very low spectral weight at the Fermi level E_F irrespectively of x , as indicated by photoemission and x-ray absorption experiments.^{20–23} Similarly, the optical conductivity $\sigma(\omega)$ shows a very low spectral weight up to an energy scale of ~ 1 eV.^{24–27} Besides, the ferromagnetic metallic phase is an atypical (bad) metal.²⁴

A physical understanding of these properties is difficult due to the internal complexity resulting from the interplay

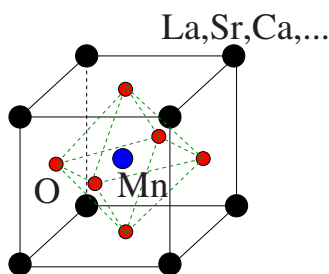


FIG. 1. (Color online) Sketch of the cubic perovskite unit cell for manganites. The dashed lines indicate the basic MnO_6 octahedron.

between charge, spin, orbital, and lattice degrees of freedom.^{28,29} A basis ingredient of a theoretical description is the separation of the electrons within the five d orbitals into a localized t_{2g} spin of length $|\mathbf{S}|=3/2$ and $n=1-x$ itinerant e_g electrons, coupled to the t_{2g} spin by Hund's exchange. This the basis of the so-called "double exchange"^{30,31} which led to the (ferromagnetic) Kondo lattice model³² and explains ferromagnetism in doped manganites and the charge-ordered phase at $x=0.5$.³³ A spin-canted state was suggested later.³⁴ However, this double exchange modeling disagrees with the experiment in many aspects including the CMR. Hence, the importance of the Jahn-Teller phonon modes and their coupling to the e_g electrons was stressed³⁵ and studied.^{36–40} However, while it can describe insulatinglike behavior for large electron-phonon coupling when electrons are trapped as lattice polarons,³⁷ the Kondo lattice model extended by Jahn-Teller phonons still fails to produce a large magnetoresistance at finite doping. Another important ingredient for the physics of manganites is the local Coulomb interaction between the e_g electrons as was pointed out in Ref. 41 and in realistic *ab initio* calculations.^{42–45} Of these *ab initio* calculations, the combination of the local density approximation (LDA) and dynamical mean field theory (DMFT) (Refs. 46–51) has the least tendency to overestimate the formation of an insulating state since the DMFT electron dynamics also avoids the cost of double occupations in the paramagnetic metallic state. The corresponding LDA+DMT results for manganites⁴⁴ show that only the combined localization effect of Coulomb interaction and (static) Jahn-Teller distortion makes the undoped parent compound an insulator, and leads to a correct description of the pressure-induced insulator-to-metal transition.¹⁷ Similarly, for the doped compound, both mechanisms work together in localizing the e_g electrons giving rise to a proper description of the unusual dynamical properties of doped manganites and the large CMR in a wide range of doping.⁵²

In this paper, we present a detailed theoretical investigation of manganites using DMFT (Refs. 53–55) to solve a realistic model of manganites which supplements the Kondo-lattice model by Jahn-Teller and breathing mode phonons as well as by the local Coulomb interaction between the e_g electrons. The paper is organized as following: Sec. II introduces

the Hamiltonian and discusses how realistic parameters are chosen. Section III is devoted to the undoped parent compound LaMnO₃ focusing in Sec. III A on how the Jahn-Teller phonons, for a cubic lattice, give rise to a very similar spectrum as that of LDA+DMFT calculations which were based on the static experimental Jahn-Teller distortion. In Sec. III B the phase transition to such a static Jahn-Teller distortion is studied and we find a similarly high transition temperature as in experiment. The distorted phase is insulating but becomes metallic upon increasing pressure. Section IV presents results for doped manganites. We focus on doping $x < 0.5$ as here electronic correlations are most relevant. In Sec. IV A a detailed study of the paramagnetic insulatinglike phase is presented and differences to the insulating phase of the parent compound are discussed. In Sec. IV B we study the phase transition toward ferromagnetism. Section V includes the effect of the breathing mode with an estimate of the Coulomb repulsion and the electron-phonon coupling strength in Sec. V A and the corresponding optical conductivity in Sec. V B. Finally, Sec. VI gives a summary of the results obtained. First results for doped manganites similar but less detailed than in Sec. IV A have been presented in Ref. 52; also see the recent DMFT calculation⁵⁶ using the semiclassical approximation as an impurity solver. Reference 56 shows qualitatively similar results—as far as this can be judged given their focus on a different doping level ($x=0.3$ instead of smaller x 's in our study).

II. REALISTIC MODEL AND PARAMETERS

For the realistic microscopic modeling of manganites, we employ the Hamiltonian

$$\begin{aligned}
 H = & - \sum_{\langle\langle ij \rangle\rangle; \mu\nu\sigma} t_{\mu\nu}^{ij} c_{i\mu\sigma}^\dagger c_{j\nu\sigma} - 2\mathcal{J} \sum_{i;\mu} \mathbf{s}_{i\mu} \cdot \mathbf{S}_i + U \sum_{i;\mu} n_{i\mu\uparrow} n_{i\mu\downarrow} \\
 & + \sum_{i;\sigma\bar{\sigma}} (U' - \delta_{\sigma\bar{\sigma}} J) n_{i1\sigma} n_{i2\bar{\sigma}} + \sum_{i;a} \left(\frac{P_{ai}^2}{2} + \frac{\Omega^2}{2} Q_{ai}^2 \right) \\
 & - g \sum_{i;\mu\nu\sigma} c_{i\mu\sigma}^\dagger (Q_{1i} \mathcal{I} + Q_{2i} \tau^x + Q_{3i} \tau^z)_{\mu\nu} c_{i\nu\sigma}. \quad (1)
 \end{aligned}$$

Here, $c_{i\mu\sigma}^\dagger$ and $c_{i\mu\sigma}$ are the fermionic creation and annihilation operators for electrons at site i within e_g orbital μ and with spin σ ; $\mathbf{s}_{i\mu}$ is the corresponding spin operator $\mathbf{s}_{i\mu} = \sum_{\sigma_1\sigma_2} c_{i\mu\sigma_1}^\dagger \frac{\tau_{\sigma_1\sigma_2}}{2} c_{i\mu\sigma_2}$ with Pauli matrices τ .

The first line of Hamiltonian (1) forms the ferromagnetic Kondo lattice model with a coupling \mathcal{J} of the e_g spin to the localized t_{2g} spin \mathbf{S}_i . For the cubic lattice, the hopping elements $t_{\mu\nu}^{ij}$ can be, to a good approximation, restricted to neighboring sites i and j in the x , y , and z directions with an orbital matrix for the two (e_g) orbitals $d_{x^2-y^2}$ and $d_{3z^2-r^2}$ indexed by μ (and ν)

$$t^x = t_0 \begin{pmatrix} \frac{3}{4} & -\frac{\sqrt{3}}{4} \\ -\frac{\sqrt{3}}{4} & \frac{1}{4} \end{pmatrix}, \quad t^y = t_0 \begin{pmatrix} \frac{3}{4} & \frac{\sqrt{3}}{4} \\ \frac{\sqrt{3}}{4} & \frac{1}{4} \end{pmatrix}, \quad (2)$$

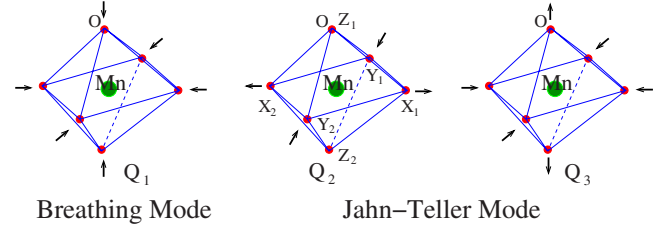


FIG. 2. (Color online) Vibration of the oxygen octahedra around the manganese ion for the breathing mode Q_1 and the two Jahn-Teller modes Q_2 and Q_3 .

$$t^z = t_0 \begin{pmatrix} 0 & 0 \\ 0 & 1 \end{pmatrix}. \quad (3)$$

The constant $t_0 = W/6 = 0.6$ eV was estimated from LDA which gives a bandwidth $W = 3.6$ eV for cubic LaMnO₃.⁴⁴ From the 2.7 eV splitting between spin-up and spin-down e_g bands in the corresponding ferromagnetic LDA calculation on the other hand, the value of coupling to the t_{2g} spins was estimated $2\mathcal{J}|\mathbf{S}_i| = 2.7$ eV.

The second line of Hamiltonian (1) describes the Coulomb repulsion of two e_g electrons on the same lattice site i , consisting of the intraorbital Coulomb repulsion U , the inter-orbital repulsion U' , and the Hund's rule energy gain J for two parallel e_g spins. The Coulomb interaction can be estimated from the experimental spectrum, combining photoemission spectroscopy and x-ray absorption spectroscopy.²³ Accounting for the crystal-field splitting between e_g states and t_{2g} states of 1–2 eV, we obtain an average Coulomb interaction $\bar{U} = 3-4$ eV, which is also supported by spectral ellipsometry for LaMnO₃.⁵⁷ Since $U' = U - 2J$ by symmetry, we have the relation

$$\bar{U} = \frac{U + U - 2J + U - 3J}{3} = U - \frac{5}{3}J. \quad (4)$$

Taking a value $J = 0.75$ eV, which is slightly smaller than the value for the five-band model obtained by constrained LDA (Ref. 58) and which agrees with our own estimate for \mathcal{J} , all Coulomb interactions are determined. Unless noted otherwise, we employ $U' = 3.5$ eV.

The third line is the Hamiltonian for the three most important phonon modes Q_a (momentum P_a) at site i , i.e., the breathing mode Q_1 and the two Jahn-Teller modes $Q_{2,3}$ as illustrated in Fig. 2. The only free parameter of this part of the Hamiltonian (1) are the three phonon frequencies which, following Ref. 59, can be obtained from the Raman spectrum for LaMnO₃. The Raman spectrum gives very similar values for the Jahn-Teller mode frequency $\Omega_{JT} = 0.07$ eV and that of the breathing mode $\Omega_{br} = 0.08$ eV so that we take a unique value $\Omega = 0.07$ eV in this paper.

Finally, the fourth line is the electron-phonon coupling with the breathing mode coupling to the electron density and the two Jahn-Teller modes coupling to the difference in e_g occupation. Avoiding to use too many parameters, we take, as for the frequency, a unique coupling strength g . For the Jahn-Teller modes it is related to the static Jahn-Teller energy $E_{JT} = g^2/2\Omega^2$, the ground-state energy if only the Jahn-Teller

coupling and phonon energy is present. One can try to determine the Jahn-Teller coupling strength g from the lattice distortion. A distortion of 0.1 \AA which is consistent with some LDA calculations^{45,60} leads to $E_{JT}=0.25 \text{ eV}$ and hence $g = 0.05 \text{ eV}^{3/2}$ for $\Omega=0.07 \text{ eV}$. However, recent x-ray powder diffraction and neutron powder-diffraction measurements found a much larger distortion,⁶¹ which would result in unrealistically large values for g or frequencies Ω at odds with the Raman frequencies. We hence attribute these larger distortions to cooperative lattice effects and the quadratic vibronic coupling to the electronic degrees of freedom. Possibly also enhancement effects due to electronic correlations play a role. As a consequence the precise value of g is an open issue and we have hence done calculations for various values of g . In Sec. V A, we provide for a new estimate of the two parameters with the biggest uncertainty, i.e., U and g on the basis of their experimental gap of undoped LaMnO_3 and the resistivity for doped LaMnO_3 .

For the following results, Hamiltonian (1) is solved using DMFT (Refs. 53–55) with Hirsch-Fye⁶² quantum Monte Carlo (QMC) simulations supplemented by the Blankenbecler-Scalapino-Sugar algorithm⁶³ for Holstein phonons. To this end, the inverse temperature β is discretized into L time slices $\tau_l = (l-1)\Delta\tau$, ($l=1, \dots, L+1$) of size $\Delta\tau = 0.25 \text{ eV}^{-1}$ and the t_{2g} spin is assumed to be classical. Let us briefly discuss some aspects of the phonon fields since these are less commonly simulated in DMFT. The phonon field can be described by a classical field ϕ_l with boundary condition $\phi_{L+1} = \phi_1$.⁶³ In the effective action, the kinetic and potential energy of the phonons [third line in Eq. (1)] hence become

$$K(\{\phi_l\}) = \frac{\Delta\tau}{2} \sum_{l=1}^L \left[\left(\frac{\phi_{l+1} - \phi_l}{\Delta\tau} \right)^2 + \Omega^2 \phi_l^2 \right]. \quad (5)$$

We employ local updates for one time slice l and global updates for all time slices, both having the form $\phi'_l = \phi_l + (x - 1/2)\delta\phi$ with a random number $x \in [0, 1)$ and a properly chosen amplitude $\delta\phi$ different for local and global updates. For low temperatures T and large electron-phonon couplings g , the probability to go through the QMC sampling from a region with large lattice distortion (occupied with one e_g electron) to a region with small lattice distortion without e_g electron becomes very low. This is quite similar to the Hubbard model where for large U and small T , the transition between configurations with predominately spin-up and spin-down becomes very rare. Fortunately, the physics in both situations is rather simple and a proper averaging between spin-up and spin-down, respectively, small and large lattice distortion is easily possible. In the latter (manganites) case, the probability $\mathcal{P}=x$ for unoccupied, undistorted sites is physical meaningful and also obtained by an extrapolation from higher temperatures.

From the DMFT one-electron spectral function the optical conductivity is calculated from the simple bubble diagram given by two Green's functions multiplied by two group velocities (derivates of the dispersion relation). For the magnetic transition temperature T_c , the two particle Green's func-

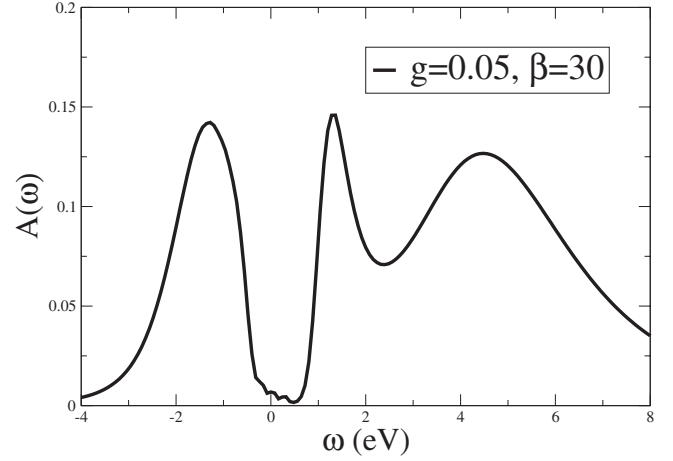


FIG. 3. Local spectral density in the paramagnetic phase of LaMnO_3 calculated for $g=0.05 \text{ eV}^{3/2}$, $U'=3.5 \text{ eV}$, and $\beta = 30 \text{ eV}^{-1}$. All other parameters are fixed as discussed in Sec. II. The breathing mode phonon will only be included later in Sec. V.

tion and from that the inverse susceptibility crossing zero at T_c were calculated.

III. INSULATING PARENT COMPOUND

A. Paramagnetic phase

We start our study with the undoped parent compound LaMnO_3 , which for a static Jahn-Teller distortion was studied in Ref. 44 using LDA+DMFT. Figure 3 shows the spin- and orbital-averaged spectral density $A(\omega) = -\frac{1}{4\pi} \sum_{\mu\sigma} \Im G^{\mu\sigma}(\omega)$ in the paramagnetic phase with the Green functions $G^{\mu\sigma}(\omega)$ obtained for real frequencies ω by the maximum entropy method.⁶⁴ It shows a three peak structure very similar to the previous LDA+DMFT results⁴⁴ even though no static Jahn-Teller distortion is present. The reason for this is that the lattice dynamics leads to a similar (averaged) lattice distortion as in the static case, see Fig. 4. At a given time shot (or for a given QMC configuration), the two

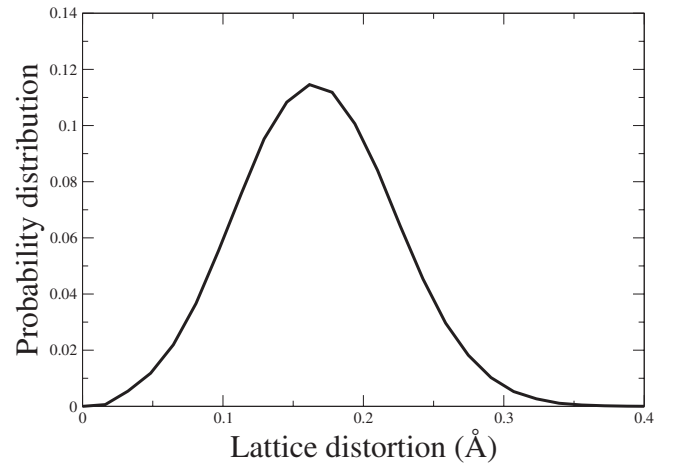


FIG. 4. Probability distribution (in arbitrary unit) of the lattice distortion for the Jahn-Teller coupling $g=0.05 \text{ eV}^{3/2}$, Coulomb repulsion $U'=3.5 \text{ eV}$ and inverse temperature $\beta=16 \text{ eV}^{-1}$.

e_g levels are Jahn-Teller split with the precise decomposition of the lower (and higher) lying orbital depending on the sign and admixture of the Q_2 and Q_3 Jahn-Teller modes. The first peak around -1.3 eV corresponds to electronic states occupying the lower of the two e_g levels and the second one around $+1.3$ eV to adding an electron in the higher lying orbital. The third peak around $+4.5$ eV corresponds to excitations to states with antiparallel t_{2g} spin, whereas the first two peaks have parallel t_{2g} spin. In Fig. 3, there is still some spectral weight in the gap which may stem from the phonon sideband.⁶⁵ The energy gap can hence only be obtained approximately. It is comparable to the experimental gap of about 1 eV.^{26,27} The consistency between the previous LDA+DMFT and the present DMFT model calculations supports our realistic microscopic model in Eq. (1) for describing the electronic behavior of LaMnO₃ and demonstrates once again that the insulating ground state in LaMnO₃ at ambient conditions results from the combination of the Coulomb interaction and the Jahn-Teller coupling in addition to the Hund's coupling between the e_g and t_{2g} spins.

Figure 4 plots the probability distribution $P(Q)$ with $Q = \sqrt{Q_2^2 + Q_3^2}$ for a given lattice distortion in the range $[Q, Q + dQ]$. Note that the lattice distortion are converted into units of Å by multiplying a factor of \hbar/\sqrt{M} , where M is the mass of oxygen atom and that for a finite $\Delta\tau$ the two modes are not exactly symmetric.

We see that $P(Q)$ has one broad peak located at around

$$\bar{Q} = \frac{\int dQ Q P(Q)}{\int dQ P(Q)} = 0.167 \text{ \AA}, \quad (6)$$

which corresponds roughly to $Q^* = g/\Omega^2 \approx 0.15$ Å obtained for a single-site model. As we have discussed, the discrepancy from the neutron experiment⁶¹ is probably due to the higher order quadratic vibronic coupling and the cooperative effect between the adjacent MnO₆ Octahedra that share a common oxygen atom.⁶⁶ A recent LDA+ U calculation has taken into account these effects and produced the correct experimental results.⁴⁵ Cluster extensions are required for further realistic DMFT calculations.

B. Structural transition

Experimentally a structural first-order phase transition is observed at $T_{OO} \approx 740$ K with an abrupt volume contraction.⁶¹ The lattice is nearly cubic above T_{OO} but has a strongly distorted orthorhombic structure due to the static Jahn-Teller distortion below T_{OO} . The structural transition is accompanied by an orbital order-disorder transition. The low-temperature phase shows a staggered ordering of the $d_{3x^2-r^2}$ and $d_{3y^2-r^2}$ orbitals in the a - b plane which repeats itself along the c direction.

With a slight modification of the single-impurity DMFT (QMC) algorithm, we can study a hypothetical antiferromagnetic orbital ordering on an AB lattice and draw some conclusions about the structural transition in LaMnO₃. To study the alternating orbital ordering, the cubic lattice is separated

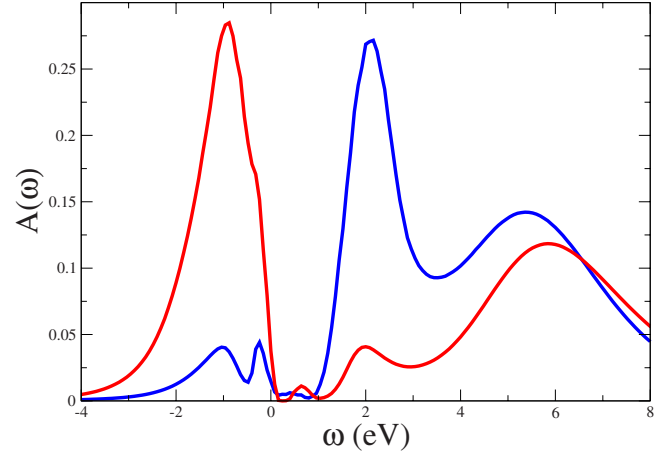


FIG. 5. (Color online) Local spectral density for the alternating orbital ordering calculated by DMFT (QMC) with the two different colors indicating the two inequivalent orbitals on a given site. The parameters are $U' = 3.5$ eV, $T = 0.05$ eV, and $g = 0.05$ eV^{3/2}.

into two sublattices A and B with opposite behavior of the two e_g orbitals: $\Sigma_{1(2)}^A(\omega) = \Sigma_{2(1)}^B(\omega)$. Due to the symmetry, we only need to take care of a single lattice site of either type in DMFT.

Figure 5 shows the local spectral densities of two e_g orbitals for $U' = 3.5$ eV, $T = 0.05$ eV, and $g = 0.05$ eV^{3/2}. At this temperature, the orbital symmetry is strongly broken: One orbital is occupied with almost one electron while the other orbital is only slightly occupied. Figure 5 also indicates the contributions from different spin and orbital components. A direct consequence of the orbital order is, due to the Jahn-Teller coupling, a corresponding lattice distortion. Averaged over the two orbital, the spectrum is actually very similar to that of Fig. 3 with the two peaks at -1 and 2 eV stemming from the spin states parallel to the local t_{2g} spins. These two peaks are split by a combination of Jahn-Teller coupling and Coulomb interaction.

Figure 6 plots the orbital polarization $P = |\sum_{\sigma} (n_{1\sigma}^A - n_{2\sigma}^A)|$, i.e., the difference of orbital occupations $n_{\mu\sigma}^A$, as a function of bandwidth and temperature. For $W = 3.6$ eV, we find a finite orbital polarization below $T \approx 725$ K, in agreement with the experimental result of the structural transition temperature $T_{OO} = 740$ K.⁶¹ If we fix the temperature $T = 0.05$ eV and vary the bandwidth as under pressure, the orbital polarization is almost a constant for the bandwidth $W < 4.8$ eV and then decreases with increasing bandwidth until it is reduced to zero at $W = 6.0$ eV. This behavior reflects the nature of the bandwidth-control metal-insulator transition in LaMnO₃. Here, $W = 4.8$ eV corresponds to the critical bandwidth where the split minority and majority e_g bands start to overlap; and LaMnO₃ becomes metallic. Hence, for a larger bandwidth, the orbital polarization decreases rapidly with increasing bandwidth.

The bandwidth $W = 6.0$ eV marks a second transition where the orbital polarization and the Jahn-Teller distortion are completely suppressed. Although different from Ref. 17, we can still identify three distinct regimes at low temperature: (i) an insulating phase with orbital ordering and static Jahn-Teller distortion below $W \approx 4.8$ eV (or $P_{IM} = 32$ GPa);

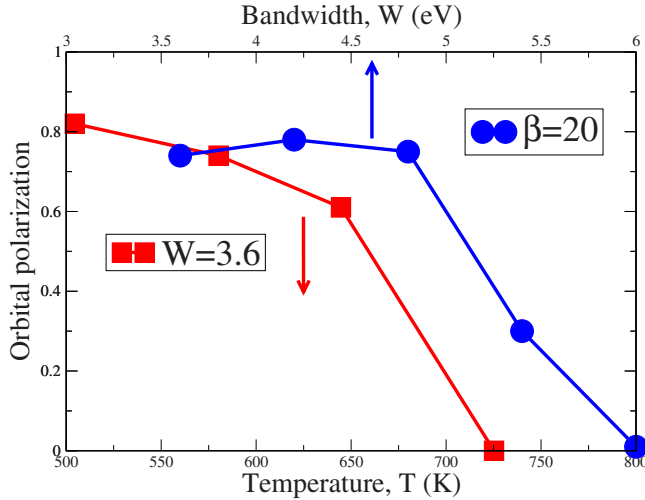


FIG. 6. (Color online) Orbital polarization vs. temperature at fixed $W=3.6$ eV (squares) and vs bandwidth at fixed $T=0.05$ eV (circles). The Jahn-Teller coupling is $g=0.05$ eV^{3/2} and the interorbital Coulomb repulsion $U'=3.5$ eV.

(ii) an intermediate metallic phase with orbital ordering and static Jahn-Teller distortion below $W \approx 6$ eV; and (iii) a metallic phase with orbital symmetry and dynamic Jahn-Teller distortion above $W \approx 6$ eV.

Hence, the Hamiltonian (1) cannot only explain the onset of orbital ordering at relatively high temperatures but also its disappearance under pressure, leading to an insulator-to-metal transition as in experiment. Hitherto, LDA+DFMT calculations⁴⁴ needed to start with the experimentally observed changes of the lattice parameters without taking into account the microscopic origin of these, i.e., the Jahn-Teller phonon modes. Let us also note that the symmetry breaking leads to a rigid shift of the two e_g bands against each other so that a band-gap insulator emerges in this situation of a static Jahn-Teller distortion. This is in striking contrast to the doped case discussed in the next section, where the dynamics of the Jahn-Teller modes result in an unusual “bad” insulator.

IV. DOPED MANGANITES

A. Paramagnetic insulating state

Let us now turn to the doped manganites with their extraordinary properties such as the colossal magnetoresistance. For simplicity, we first neglect the breathing phonon mode. We start by plotting the probability distribution of the lattice distortion for $n=0.8$ ($x=0.2$) at different temperatures and couplings in Fig. 7. The Coulomb interaction is fixed to $U'=3.5$ eV throughout Sec. IV. In contrast to the single-peak distribution obtained for the undoped case in Fig. 4, we find two peaks in the distribution function at large Jahn-Teller couplings for doped systems. The large peak located at about g/Ω^2 corresponds to the large lattice distortion due to the Jahn-Teller coupling (and corresponds to the single peak without doping) while the small peak stems from the quantum and thermal fluctuation of the MnO_6 octahedra which due to the doping are not occupied with an electron (and hence not strongly split by the electron-phonon coupling g).

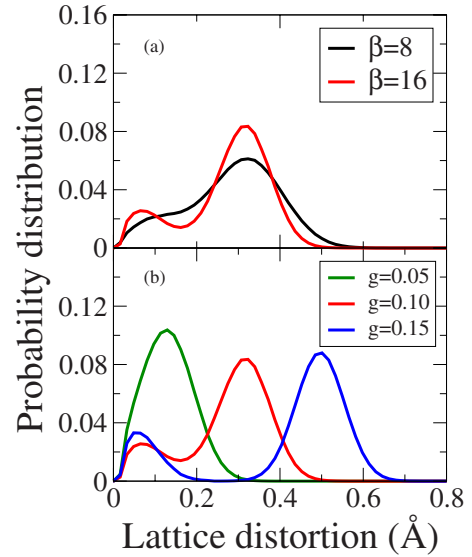


FIG. 7. (Color online) Probability distribution of the lattice distortion at $n=0.8$ e_g electrons per site (i.e., doping $x=0.2$) for (a) $g=0.10$ eV^{3/2} and $\beta=8$ and 16 eV⁻¹, and (b) $\beta=16$ eV⁻¹ and $g=0.05, 0.10$, and 0.15 eV^{3/2}. (Note that in contrast to Fig. 1 of Ref. 52, the distortion due to both Jahn-Teller modes $Q=\sqrt{Q_2^2+Q_3^2}$ is shown.)

While at a large coupling strength $g \geq 0.1$, the two peaks are well separated, they merge into a single structure at weak coupling such as for $g=0.05$ eV^{3/2} in Fig. 4.

The connection to the electronic spectrum is shown in Fig. 8. For clarity, we separate the spectrum into two parts originated from the large and small lattice distortions, respectively. For the large lattice distortion, the corresponding spectral density locates well below or far above the Fermi energy. The low-energy part can be identified as localized e_g electrons or more precisely the transition from this state to states without e_g electron. The high-energy part stems from the states which are pushed up by the Hund’s rule coupling, the Jahn-Teller splitting, and the Coulomb repulsion. For the small lattice distortion, most of the spectral density locates slightly above the Fermi energy. They stem from the “undistorted” unoccupied states which are also called “midgap states” in the literature.^{26,37}

The formation of lattice polarons provides for the basic physics of doped manganites. The electron spectral density can be seen as a combination of polaron states well below the Fermi energy and the midgap states above the Fermi energy. As shown in Fig. 8, this results in the strong suppression of the spectral weight at the Fermi energy and gives rise to a large energy gap for $g=0.15$ eV^{3/2} and a pseudogap for smaller Jahn-Teller couplings.

Let us discuss the role of the on-site Coulomb interaction in the formation of the pseudo gap and hence the insulating-like paramagnetic state of manganites. Figure 9 compares the spectral densities for $g=0.10$ eV^{3/2} with and without the Coulomb interaction; Fig. 8 the corresponding probability distribution of the lattice distortion. For $U=5$ eV ($U'=3.5$ eV), some spectral weight is pushed away from the Fermi energy to higher energies and the pseudogap is strongly enhanced by the Coulomb interaction. Also the lat-

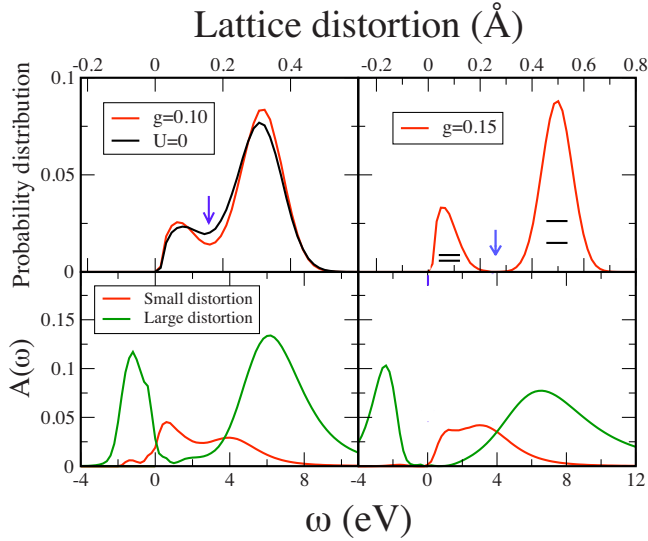


FIG. 8. (Color online) Probability distribution of the lattice distortion and the corresponding electron spectral densities for the Jahn-Teller coupling $g=0.10$ eV^{3/2} (left panel) and 0.15 (right panel) at inverse temperature $\beta=16$ eV⁻¹ and $n=0.8$ e_g electrons per site. The electron spectral densities (lower two panels) are separated into two parts with large and small lattice distortions. The lattice distortion below which the spectral contribution is counted as small distortion (red/dark gray line in the lower panels) and above which as large distortion (green/light gray line) is marked by an arrow in the two respective upper panels. The phonon distribution at $g=0.10$ eV^{3/2} without the Coulomb interaction is also shown for comparison.

tice distortion shows a more pronounced separation of the two peaks which indicates the enhancement of the polaron formation by the Coulomb interaction. This confirms the important role of the Coulomb interaction.

Let us now consider the gradual switching on of the Jahn-Teller couplings g at fixed $\beta=16$ eV⁻¹ and $n=0.8$ shown in Fig. 10. Without Jahn-Teller coupling, the spectrum has a broad quasiparticle peak at the Fermi energy and the system is metallic. With increasing g , the quasiparticle peak is

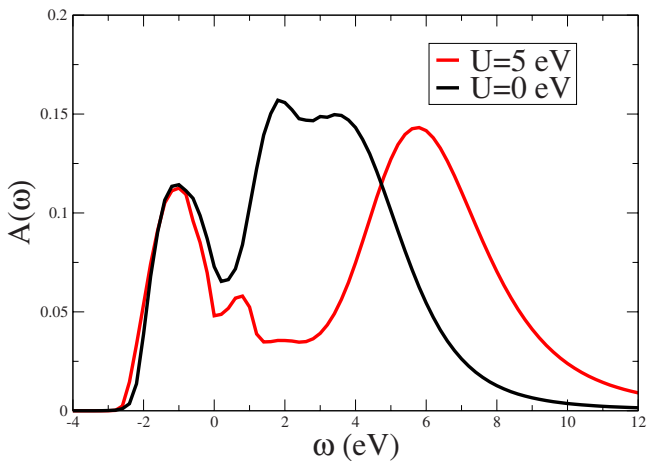


FIG. 9. (Color online) Paramagnetic electronic spectral density at $n=0.8$, $\beta=16$ eV⁻¹, and $g=0.10$ eV^{3/2} comparing $U=0$ eV and $U=5$ eV ($U'=3.5$ eV).

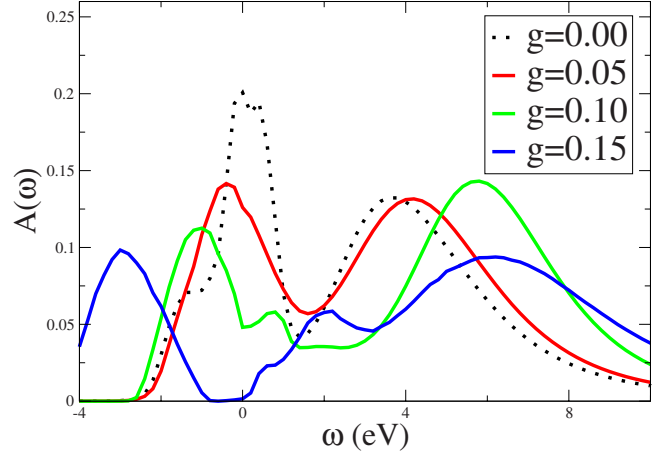


FIG. 10. (Color online) Electron spectral density in the paramagnetic phase for different couplings $g=0, 0.05, 0.10,$ and 0.15 eV^{3/2}. The parameters are $\beta=16$ eV⁻¹ and $n=0.8$. The quasiparticle peak is suppressed at large g , giving the pseudogap behavior for intermediate coupling and a large energy gap for strong coupling.

gradually suppressed and the spectral weight at the Fermi energy is reduced, leaving a dip in the spectrum for intermediate coupling and an energy gap for strong coupling. The low- (high-) energy Hubbard band also shifts toward lower (higher) energies. An additional peak shows up at $\omega = 1-2$ eV, ascribed to the midgap states with small dynamic lattice distortion.

Turning to the doping dependence at fixed $\beta=16$ eV⁻¹ and $g=0.10$ eV^{3/2} in Fig. 11, we see that the system is a good insulator with a large energy gap of about 2.3 eV without doping. This is larger than the experimental gap of 1 eV and hence suggests that a smaller Jahn-Teller coupling such as $g=0.05$ eV^{3/2} used in Sec. III is more realistic. But for the qualitative discussion here, we continue with $g=0.1$ eV^{3/2} since for this larger Jahn-Teller coupling the different features of the spectrum can be better identified. A small doping $x=0.1$ introduces some midgap states just above the Fermi

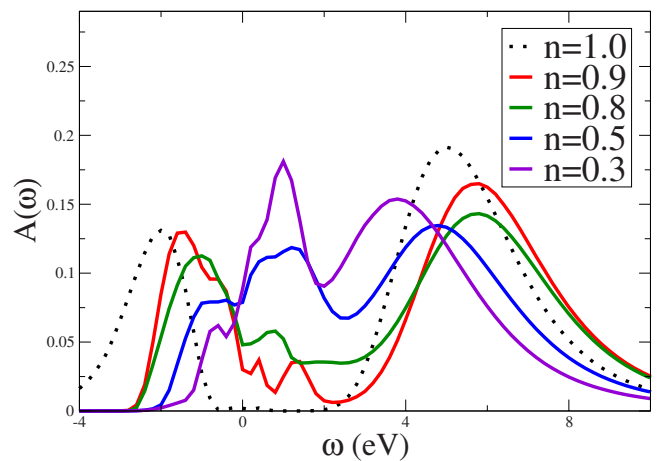


FIG. 11. (Color online) Paramagnetic spectral density for different electron occupations $n=1.0, 0.9, 0.8, 0.5,$ and 0.3 at $\beta=16$ eV⁻¹ and $g=0.10$ eV^{3/2}.

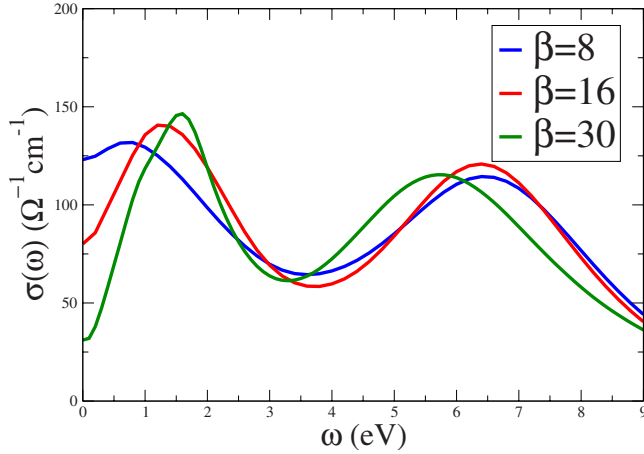


FIG. 12. (Color online) Optical conductivity in the paramagnetic phase at average occupancy $n=0.8$ and inverse temperature $\beta=8, 16,$ and 30 eV^{-1} .

energy and changes the large energy gap into a pseudogap at the Fermi energy. If the doping is large enough, the midgap states can dominate at the Fermi energy so that the pseudogap is completely filled at $n=0.3$. However, due to the strong phonon and spin scattering, the quasiparticle peak is still damped (broadened); i.e., the lifetime of the quasiparticles is very short. This physical situation can give rise to an insulatinglike increase in the resistivity with decreasing temperature see Fig. 18 below, also see the following discussion of the T dependence of the optical conductivity in the next paragraph and Fig. 12. But as the spectrum, Fig. 11, clearly shows, the state is entirely different from the normal (gapped) insulator we find for the undoped parent compound ($n=1$).

Since the temperature dependence of the spectrum was already discussed in Ref. 52, we restrict ourselves here to the optical conductivity in Fig. 12. The low energy optical conductivity is suppressed as a result of the pseudogap in the spectral density. With decreasing temperature, the optical spectrum is more suppressed since there are less thermal excitations and the two peak lattice distortion becomes more pronounced (Fig. 7) as does the pseudogap.⁵² Hence, the resistivity is enhanced at low temperature, giving rise to the insulating behavior in the paramagnetic phase, see Ref. 52 for the T dependence of the resistivity.

The two peaks of the optical spectrum stem from the two peaks in the electronic spectrum above their Fermi energy. An excitation of an electron into the unoccupied, undistorted states just above the Fermi energy gives rise to the midgap states around 1.5 eV. Transitions to the distorted states far above the Fermi energy with two e_g electrons are at the origin of the peak around 6 eV.

B. Ferromagnetic phase transition

The low-temperature ferromagnetic phase is a bad metal which due to the strong spin and phonon scattering has quasiparticles with very short lifetimes and no true Drude peak.⁵² Here, we will concentrate on the ferromagnetic phase transition which can be either driven by applying a magnetic

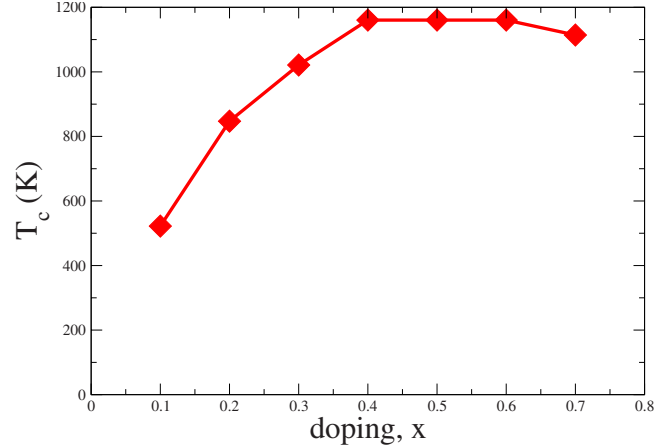


FIG. 13. (Color online) Curie temperature as a function of doping $x=1-n$ for $g=0.10 \text{ eV}^{3/2}$.

field or by decreasing the temperature. Figure 13 shows the doping dependence of the Curie temperature for the Jahn-Teller coupling $g=0.10 \text{ eV}^{3/2}$. Compared to the experimental results, the theoretical predictions of T_c have a similar shape with a maximum at intermediate doping but overall the values of T_c are about two to three times larger in magnitude. Close to the undoped parent compound ($x=0, n=1$), the Curie temperature is suppressed since the Coulomb interaction hinders the movement of the electrons so that the double exchange is no longer effective; instead antiferromagnetism prevails.⁴¹

The magnitude of the Curie temperature depends strongly on the strength of the Jahn-Teller coupling and the hopping integral of the e_g electrons. Figure 14 plots its coupling dependence at $n=0.8$, which are similar to the previous results.^{39,65} The Curie temperature decreases rapidly with increasing coupling. For strong Jahn-Teller coupling, a slight increase of g from 0.10 to 0.12 (or the dimensionless coupling λ from 2.0 to 2.2) reduces T_c by a factor of 2 so that $g=0.12 \text{ eV}^{3/2}$ (or $\lambda=2.2$) gives the correct experimental value.

The Curie temperature may also be affected by many factors which are not included in our low-energy Hamiltonian.

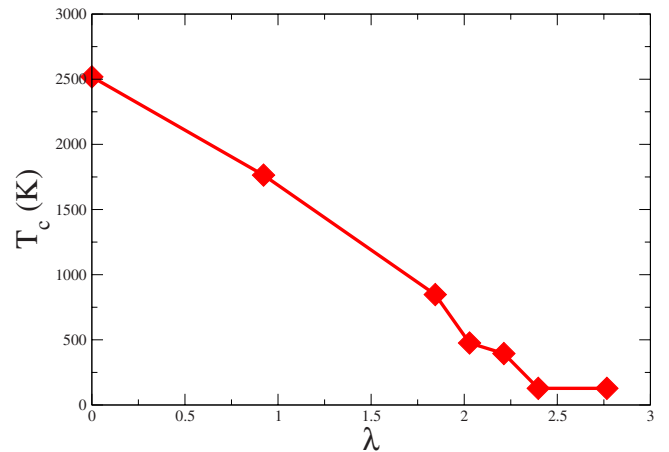


FIG. 14. (Color online) Curie temperature as a function of the dimensionless coupling $\lambda=g/\Omega\sqrt{t_0}$ at $n=0.8$.

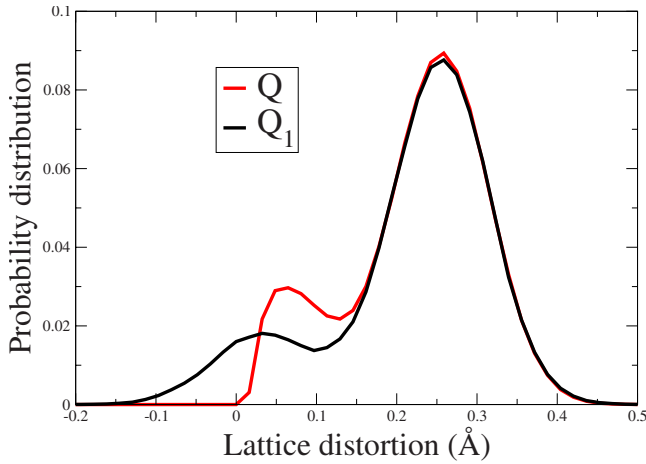


FIG. 15. (Color online) Probability distribution of the breathing (Q_1) and Jahn-Teller (Q) modes for the model Hamiltonian (1). The parameters are $n=0.8$ and $\beta=16$ eV $^{-1}$, $U=5$ eV, $U'=3.5$ eV, $J=0.75$ eV, $g=0.08$ eV $^{3/2}$, and $\Omega=0.07$ eV for all three modes.

These include the quantum fluctuation of Mn t_{2g} spins and the antiferromagnetic superexchange coupling between Mn t_{2g} spins. Both tend to weaken the ferromagnetic order and suppress the Curie temperature. The antiferromagnetic superexchange coupling has been estimated to be the order of 200 K (Refs. 16 and 67) which, if taken into account, would greatly reduce the theoretical value of the Curie temperature. Also the mean field character of the DMFT approximation tends to overestimate the Curie temperature.

In the literature, the Curie temperature has been calculated with different methods such as DMFT,^{35,37,41} conventional mean field theory,³⁶ QMC simulations,⁶⁸ and the many-body coherent potential approximation.⁶⁵ Some of the results seem to be in better agreement with experiments. However, we should note that these results are all based on the details of the models and approaches and are very sensitive to the values of the parameters which, unfortunately, are not always reliable and, as a matter of fact, vary considerably in the literature. A complete analysis of the problem is still required.

V. BREATHING MODE

In this section we include a third electron-phonon coupling, the breathing mode which couples to the electron density, see Sec. II. Figure 15 shows the probability distribution of both the breathing and Jahn-Teller phonon fields at $\beta=16$ eV $^{-1}$, $n=0.8$, $g=0.08$ eV $^{3/2}$, $U=5$ eV, $J=0.75$ eV, and $U'=3.5$ eV, and a phonon frequency $\Omega=0.07$ eV for all three modes. Except for the Jahn-Teller distortion Q being positive by definition, the distribution function of the breathing phonon is similar to that of the Jahn-Teller distortion and also has two peaks located at about g/Ω^2 and 0. These two peaks are related to the polaron states and the midgap states discussed before. The only difference is the way in which the phonon modes are coupled to the e_g electrons: the breathing mode is coupled to the electron density, while the Jahn-Teller modes are coupled to the orbital polarization (with respect to

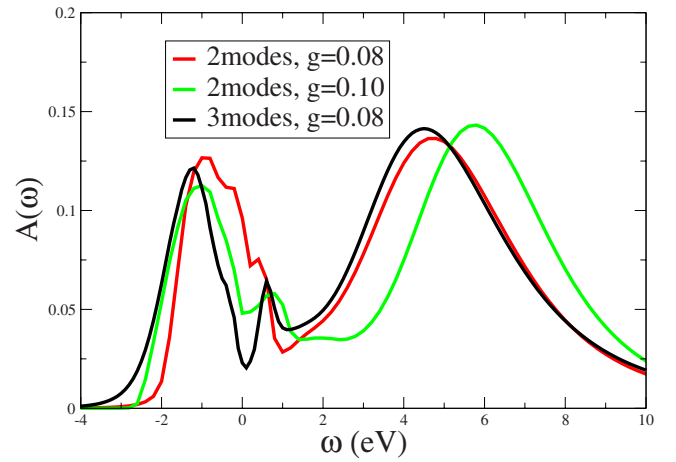


FIG. 16. (Color online) Electron spectral density for $U'=3.5$ eV, $n=0.8$, and $\beta=16$ eV $^{-1}$. The coupling constant is taken as $g=0.08$ eV $^{3/2}$ for calculations with all three phonon modes and $g=0.08, 0.10$ eV $^{3/2}$ for calculations with only the Jahn-Teller modes. The phonon frequencies are taken as $\Omega=0.07$ eV for all three modes.

a certain basis). Due to the Hund's coupling and the strong Coulomb interaction, double occupations are forbidden. Hence, the difference is not reflected in the distribution function.

Since the breathing mode only couples to the electron density, it lowers the localization energy of the polaron states but leaves the midgap states unchanged. The e_g electrons are thus more localized due to the inclusion of the breathing mode and the system becomes more insulating.

Figure 16 compares the spectral densities at $\beta=16$ eV $^{-1}$ and $n=0.8$ with and without the breathing phonon. As expected, we see the density of states at the Fermi energy to be strongly suppressed by the existence of the breathing mode, demonstrating how the breathing mode supports the tendencies toward localization of the e_g electrons.

A. Determining U and g

Let us now try to estimate from our results including the breathing mode the two parameters with the hitherto largest uncertainty, i.e., the on-site Coulomb interaction U and the electron-phonon coupling g . All other parameters are fixed as discussed in Sec. II. To this end, we fit the two parameters to two experimental values, i.e., the experimental gap of undoped LaMnO $_3$ which is 1 eV and the resistivity for $x=17.5\%$ Sr doping which is 0.035 Ω cm. The calculations are done for $\beta=30$ eV $^{-1}$.

The inset (a) of Fig. 17 plots the energy gap for different Coulomb interactions U and Jahn-Teller couplings g calculated by DMFT (QMC) for the model Hamiltonian (1). As expected, the energy gap depends strongly on both parameters.

The inset (b) of Fig. 17 shows the DMFT (QMC) results of the resistivity for different U and g at $n=0.825$ ($x=0.175$) and $\beta=30$ eV $^{-1}$. As has been analyzed before, the Coulomb interaction also affects the resistivity of the system since it enhances the electron localization. This is now

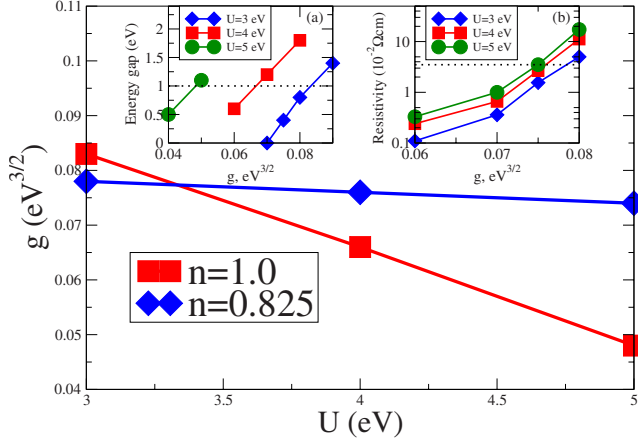


FIG. 17. (Color online) Two sets of parameters which fit the experimental energy gap in LaMnO_3 and the resistivity in $\text{La}_{0.825}\text{Sr}_{0.175}\text{MnO}_3$. Their intersection gives a single set (U, g) which is expected to describe quantitatively both doped and undoped manganites. The insets show the DMFT (QMC) results as a function of the Coulomb interaction U and the Jahn-Teller coupling g for: (a) the energy gap at $n=1$ and (b) the resistivity at $n=0.825$. Both are calculated at $\beta=30 \text{ eV}^{-1}$. The experimental results are indicated by the dotted line with the 1 eV energy gap in LaMnO_3 and the resistivity of about $0.035 \text{ } \Omega \text{ cm}$ for $\text{La}_{0.825}\text{Sr}_{0.175}\text{MnO}_3$ (Refs. 4 and 5).

proved explicitly in the figure. The resistivity increases with increasing U , albeit it depends more sensitive on g than on U .

By comparing with the experimental data (dotted lines in the two insets), the two experiments provide for two different sets of U and g parameters which we plot in the main panel of Fig. 17. Only the intersection at $U=3.3 \text{ eV}$ and $g=0.077 \text{ eV}^{3/2}$ agrees with both experiments. These parameters determined by us agree with the crude estimates of Sec. II. We hence expect this parameter set, summarized in Table I, to be the proper set for the model Hamiltonian (1), describing both doped and undoped manganites.

As an additional test, suggested to us and carried out *a posteriori*, we study the change of the resistivity with temperature and that from the paramagnetic to the ferromagnetic phase in Fig. 18. Both changes basically agree with experiment, i.e., at the experimental Curie temperature a similar jump in resistivity when going from the paramagnetic to the

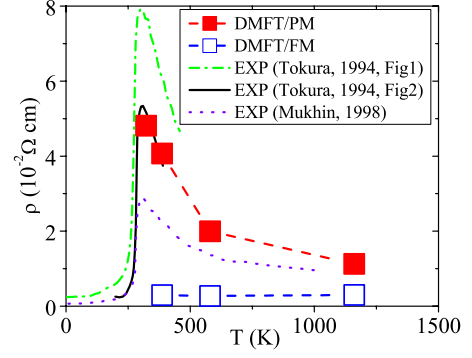


FIG. 18. (Color online) Resistivity of $\text{La}_{0.825}\text{Sr}_{0.175}\text{MnO}_3$ as a function of temperature comparing LDA+DMFT with three experimental figures from Refs. 4 and 12, respectively. All parameters have been determined *a priori* and are summarized in Table I ($n=0.825$). Within the experimental ambiguity, our theoretical results agree both in the insulatinglike increase in the paramagnetic (PM) resistivity with decreasing temperature and the colossal drop in resistivity upon entering the ferromagnetic (FM) phase.

ferromagnetic phase is found.⁶⁹ Indeed the largest source of ambiguity appears to be the experimental uncertainty of a factor 2–3 in the resistivity. There are several potential origins of the rather different experimental resistivities: (i) the exact doping level x is difficult to control; (ii) the samples might have irregular shapes; and (iii) scattering at grain boundary. Fortunately this experimental uncertainty only translates into rather tiny uncertainties in the determined Coulomb and Jahn-Teller interactions: $\delta U \sim 0.2 \text{ eV}$ and $\Delta g \sim 0.002 \text{ eV}^{3/2}$.

This shows that both Coulomb interaction *and* electron-phonon coupling need to be included, in agreement with^{41,44,52,56} but in contrast to earlier theoretical calculations based on the electron-phonon coupling alone.^{35,37–39} Without Coulomb interaction, a sizeable change in resistivity when going from the paramagnetic to the ferromagnetic phase could indeed only be described at quarter filling ($n=1$) whereas in experiment and in our calculations, see, e.g., Fig. 18, the CMR is found in a large doping range.

B. Optical conductivity

The optical conductivity with the breathing mode included for the determined set of parameters is presented in

TABLE I. Parameters estimated for doped and undoped manganites. $W=6t_0$: bandwidth; U : intraorbital Coulomb interaction; J : e_g - e_g Hund's exchange; \mathcal{J} : e_g - t_{2g} Hund's coupling; Ω : phonon frequency; and g : Jahn-Teller coupling. The bandwidth is obtained from the LDA calculations for the cubic structure (Ref. 44), the Hund's coupling is calculated by the constrained LDA for the ferromagnetic phase, and the phonon frequency is estimated from the Raman spectroscopy (Ref. 59). Only the Coulomb interaction U and the Jahn-Teller coupling g are estimated from the DMFT (QMC) calculations for the model Hamiltonian (1) by fitting the experimental data of the energy gap in LaMnO_3 and the resistivity in $\text{La}_{0.825}\text{Sr}_{0.175}\text{MnO}_3$, see Fig. 17.

W (eV)	U (eV)	$2\mathcal{J} S $ (eV)	J (eV)	Ω (eV)	g ($\text{eV}^{3/2}$)
3.6	3.3	2.7	0.75	0.07	0.077

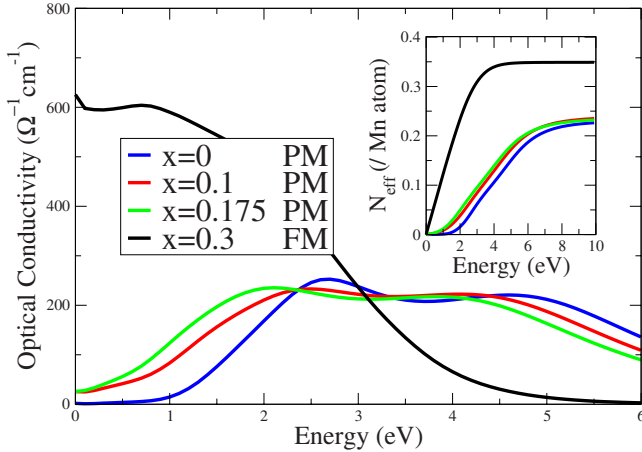


FIG. 19. (Color online) Optical conductivity at doping $x=0, 0.1$, and 0.175 in the PM phase and at $x=0.3$ in the FM phase. The parameters are taken as is in Table I and the inverse temperature is $\beta=30 \text{ eV}^{-1}$. The inset shows the effective carrier concentration calculated from the integrated optical conductivity.

Fig. 19. The inset is the effective carrier concentration $N_{\text{eff}}(\omega)$ calculated from the integral of the optical conductivity which can be compared directly to the experimental results of Ref. 27. We see a continuous crossover from the undoped to the doped system and a good agreement in the general behavior of the optical conductivity with experiment. However, the experimental magnitude of the optical peaks are two to three times larger than the theoretical one.²⁵ This gives rise to an unexpected large experimental $N_{\text{eff}}(\omega)$ even below 4 eV, in contrast to the theoretical predictions presented in the inset of Fig. 19. This suggests that, besides the e_g states also oxygen p and Mn t_{2g} states which we did not account for in the theoretical calculation contribute to the experimental optical conductivity. Another possible explanation is the insufficiency of the group velocity as a substitute for the more appropriate dipole matrix elements.

VI. CONCLUSION

We have used DMFT to study the physics of manganites by hands of a realistic microscopic model which takes into account both the electron-electron and electron-phonon interactions, together with the Hund's rule coupling between the e_g conduction electrons and the t_{2g} spins. In the undoped system, the model produces similar results as the previous LDA+DMFT calculations and, most surprisingly, it also predicts the correct structural transition temperature from dynamic to static Jahn-Teller distortion. In the doped phase, the e_g electrons are trapped by the large lattice distortion and

form a lattice polarons. This process is strongly supported by the Coulomb interaction. Our results provide for an explanation of the insulatinglike paramagnetic state over a wide range of doping. The CMR is a result of a transition toward a ferromagnetic (bad) metallic state at a Curie temperature which shifts by applying an external magnetic field. The dynamical properties are determined by the polaron states and midgap states which stem from the undistorted unoccupied states slightly above the Fermi energy. The combination of both gives rise to the pseudogap behavior observed in doped manganites. The inclusion of the breathing mode further favors the tendencies toward polaron formation. Our results show that the realistic microscopic model can be applied to both doped and undoped manganites and can therefore be taken as the starting point toward a complete understanding of the physics of manganites. For future studies we provide for a realistic set of model parameters in Table I.

Let us finally discuss the most important terms neglected and the limitations of the calculations. The most important terms not taken into account in our study, also see, Ref. 56, are: (i) a cooperative Jahn-Teller term coupling Jahn-Teller phonons on adjacent sites which will further support the tendencies toward structural phase transition, which we discussed in Sec. III B. (ii) The (antiferromagnetic) superexchange coupling between the t_{2g} spins which will reduce the critical (ferromagnetic) transition temperature calculated in Sec. IV B but will, as the cooperative Jahn-Teller term, otherwise hardly affect the results within DMFT, in particular not in the paramagnetic phase.

For a three-dimensional system as the manganites DMFT (which we solve numerically exactly by QMC) is reliable in the paramagnetic phase since nonlocal correlations become important only in the immediate vicinity of a phase transition.^{70,71} The critical temperatures for these phase transitions on the other hand are quite substantially overestimated by $\sim 30\%$. Together with the expected effects of the aforementioned neglected terms in the Hamiltonian, we can hence conclude that the biggest limitations of our calculations concern the phase transitions toward long-range orbital or magnetic ordering. This can be improved upon by extending the Hamiltonian and by going beyond DMFT, e.g., by cluster⁷⁰ or diagrammatic extensions.^{72,73}

ACKNOWLEDGMENTS

This work has been supported by the EU-Indian cooperative FP-7 network MONAMI and the FWF through SFB ViCom F41 and Research Unit FOR 1346; work at Los Alamos was performed under the auspices of the U.S. Department of Energy. We thank A. Pimenov for discussions concerning the experimental uncertainty in the resistivity.

- ¹R. von Helmolt, J. Wecker, B. Holzapfel, L. Schultz, and K. Samwer, *Phys. Rev. Lett.* **71**, 2331 (1993).
- ²K. Chahara, T. Ohno, M. Kasai, and Y. Kozono, *Appl. Phys. Lett.* **63**, 1990 (1993).
- ³S. Jin, T. H. Tiefel, M. McCormack, R. A. Fastnacht, R. Ramesh, and L. H. Chen, *Science* **264**, 413 (1994).
- ⁴Y. Tokura, A. Urushibara, Y. Moritomo, T. Arima, A. Asamitsu, G. Kido, and N. Furukawa, *J. Phys. Soc. Jpn.* **63**, 3931 (1994).
- ⁵A. Urushibara, Y. Moritomo, T. Arima, A. Asamitsu, G. Kido, and Y. Tokura, *Phys. Rev. B* **51**, 14103 (1995).
- ⁶H. Kuwahara, Y. Tomioka, A. Asamitsu, Y. Moritomo, and Y. Tokura, *Science* **270**, 961 (1995).
- ⁷Y. Tomioka, A. Asamitsu, Y. Moritomo, H. Kuwahara, and Y. Tokura, *Phys. Rev. Lett.* **74**, 5108 (1995).
- ⁸Y. Tomioka, A. Asamitsu, Y. Moritomo, and Y. Tokura, *J. Phys. Soc. Jpn.* **64**, 3626 (1995).
- ⁹Y. Tomioka, A. Asamitsu, H. Kuwahara, Y. Moritomo, and Y. Tokura, *Phys. Rev. B* **53**, R1689 (1996).
- ¹⁰Y. Tomioka, A. Asamitsu, H. Kuwahara, and Y. Tokura, *J. Phys. Soc. Jpn.* **66**, 302 (1997).
- ¹¹Y. Moritomo, H. Kuwahara, Y. Tomioka, and Y. Tokura, *Phys. Rev. B* **55**, 7549 (1997).
- ¹²A. A. Mukhin, V. Y. Ivanov, V. D. Travkin, S. P. Lebedev, A. Pimenov, A. Loidl, and A. M. Balbashov, *Pis'ma Zh. Eksp. Teor. Fiz.* **68**, 331 (1998); [*JETP Lett.* **68**, 356 (1998)].
- ¹³Y. Tokura, Y. Tomioka, H. Kuwahara, A. Asamitsu, Y. Moritomo, and M. Kasai, *J. Appl. Phys.* **79**, 5288 (1996).
- ¹⁴Y. Tokura and Y. Tomioka, *J. Magn. Magn. Mater.* **200**, 1 (1999).
- ¹⁵M. B. Salamon and M. Jaime, *Rev. Mod. Phys.* **73**, 583 (2001).
- ¹⁶E. Dagotto, T. Hotta, and A. Moreo, *Phys. Rep.* **344**, 1 (2001).
- ¹⁷I. Loa, P. Adler, A. Grzechnik, K. Syassen, U. Schwarz, M. Hanfland, G. K. Rozenberg, P. Gorodetsky, and M. P. Pasternak, *Phys. Rev. Lett.* **87**, 125501 (2001).
- ¹⁸Y. Tomioka and Y. Tokura, *Phys. Rev. B* **70**, 014432 (2004).
- ¹⁹R. Mathieu *et al.*, *Phys. Rev. B* **74**, 020404(R) (2006).
- ²⁰A. E. Bocquet, T. Mizokawa, T. Saitoh, H. Namatame, and A. Fujimori, *Phys. Rev. B* **46**, 3771 (1992).
- ²¹A. Chainani, M. Mathew, and D. D. Sarma, *Phys. Rev. B* **47**, 15397 (1993).
- ²²T. Saitoh, A. Sekiyama, K. Kobayashi, T. Mizokawa, A. Fujimori, D. D. Sarma, Y. Takeda, and M. Takano, *Phys. Rev. B* **56**, 8836 (1997).
- ²³J.-H. Park, C. T. Chen, S.-W. Cheong, W. Bao, G. Meigs, V. Chakarian, and Y. U. Idzerda, *Phys. Rev. Lett.* **76**, 4215 (1996).
- ²⁴Y. Okimoto, T. Katsufuji, T. Ishikawa, A. Urushibara, T. Arima, and Y. Tokura, *Phys. Rev. Lett.* **75**, 109 (1995).
- ²⁵M. Quijada, J. Černe, J. R. Simpson, H. D. Drew, K. H. Ahn, A. J. Millis, R. Shreekala, R. Ramesh, M. Rajeswari, and T. Venkatesan, *Phys. Rev. B* **58**, 16093 (1998).
- ²⁶J. H. Jung, K. H. Kim, T. W. Noh, E. J. Choi, and J. Yu, *Phys. Rev. B* **57**, R11043 (1998).
- ²⁷K. Takenaka, K. Iida, Y. Sawaki, S. Sugai, Y. Moritomo, and A. Nakamura, *J. Phys. Soc. Jpn.* **68**, 1828 (1999).
- ²⁸A. J. Millis, *Nature (London)* **392**, 147 (1998).
- ²⁹Y. Tokura, *Phys. Today* **56**(7), 50 (2003).
- ³⁰C. Zener, *Phys. Rev.* **81**, 440 (1951).
- ³¹C. Zener, *Phys. Rev.* **82**, 403 (1951).
- ³²K. Kubo and N. Ohata, *J. Phys. Soc. Jpn.* **33**, 21 (1972).
- ³³J. B. Goodenough, *Phys. Rev.* **100**, 564 (1955).
- ³⁴P.-G. de Gennes, *Phys. Rev.* **118**, 141 (1960).
- ³⁵A. J. Millis, P. B. Littlewood, and B. I. Shraiman, *Phys. Rev. Lett.* **74**, 5144 (1995).
- ³⁶H. Röder, J. Zang, and A. R. Bishop, *Phys. Rev. Lett.* **76**, 1356 (1996).
- ³⁷A. J. Millis, B. I. Shraiman, and R. Mueller, *Phys. Rev. Lett.* **77**, 175 (1996).
- ³⁸A. J. Millis, R. Mueller, and B. I. Shraiman, *Phys. Rev. B* **54**, 5389 (1996).
- ³⁹A. J. Millis, R. Mueller, and B. I. Shraiman, *Phys. Rev. B* **54**, 5405 (1996).
- ⁴⁰Let us also note F. Zhong, J. Dong, and Z. D. Wang, *Phys. Rev. B* **58**, 15310 (1998) which discusses the effect of disorder and assumes that every La-ion substituted, e.g., by Sr changes the local potential of one Mn site.
- ⁴¹K. Held and D. Vollhardt, *Phys. Rev. Lett.* **84**, 5168 (2000).
- ⁴²G. Banach and W. M. Temmerman, *J. Phys.: Condens. Matter* **16**, S5633 (2004).
- ⁴³H. Zenia, G. A. Gehring, and W. M. Temmerman, *New J. Phys.* **7**, 257 (2005).
- ⁴⁴A. Yamasaki, M. Feldbacher, Y.-F. Yang, O. K. Andersen, and K. Held, *Phys. Rev. Lett.* **96**, 166401 (2006).
- ⁴⁵W. Yin, D. Volja, and W. Ku, *Phys. Rev. Lett.* **96**, 116405 (2006).
- ⁴⁶V. I. Anisimov, A. I. Poteryaev, M. A. Korotin, A. O. Anokhin, and G. Kotliar, *J. Phys.: Condens. Matter* **9**, 7359 (1997).
- ⁴⁷A. I. Lichtenstein and M. I. Katsnelson, *Phys. Rev. B* **57**, 6884 (1998).
- ⁴⁸M. I. Katsnelson and A. I. Lichtenstein, *Phys. Rev. B* **61**, 8906 (2000).
- ⁴⁹K. Held, I. Nekrasov, G. Keller, V. Eyert, N. Blümer, A. K. McMahan, R. T. Scalettar, T. Pruschke, V. I. Anisimov, and D. Vollhardt, *Physica B* **243**, 2599 (2006).
- ⁵⁰G. Kotliar, S. Y. Savrasov, K. Haule, V. S. Oudovenko, O. Parcollet, and C. Marianetti, *Rev. Mod. Phys.* **78**, 865 (2006).
- ⁵¹K. Held, *Adv. Phys.* **56**, 829 (2007).
- ⁵²Y.-F. Yang and K. Held, *Phys. Rev. B* **76**, 212401 (2007).
- ⁵³W. Metzner and D. Vollhardt, *Phys. Rev. Lett.* **62**, 324 (1989).
- ⁵⁴A. Georges and G. Kotliar, *Phys. Rev. B* **45**, 6479 (1992).
- ⁵⁵A. Georges, G. Kotliar, W. Krauth, and M. J. Rozenberg, *Rev. Mod. Phys.* **68**, 13 (1996).
- ⁵⁶C. Lin and A. J. Millis, *Phys. Rev. B* **78**, 174419 (2008).
- ⁵⁷N. N. Kovaleva, A. V. Boris, C. Bernhard, A. Kulakov, A. Pimenov, A. M. Balbashov, G. Khaliullin, and B. Keimer, *Phys. Rev. Lett.* **93**, 147204 (2004).
- ⁵⁸S. Satpathy, Z. S. Popović, and F. R. Vukajlović, *Phys. Rev. Lett.* **76**, 960 (1996).
- ⁵⁹M. N. Iliev, M. V. Abrashev, H.-G. Lee, V. N. Popov, Y. Y. Sun, C. Thomsen, R. L. Meng, and C. W. Chu, *Phys. Rev. B* **57**, 2872 (1998).
- ⁶⁰W. E. Pickett and D. J. Singh, *Phys. Rev. B* **53**, 1146 (1996).
- ⁶¹T. Chatterji, F. Fauth, B. Ouladdiaf, P. Mandal, and B. Ghosh, *Phys. Rev. B* **68**, 052406 (2003).
- ⁶²J. E. Hirsch and R. M. Fye, *Phys. Rev. Lett.* **56**, 2521 (1986).
- ⁶³R. Blankenbecler, D. J. Scalapino, and R. L. Sugar, *Phys. Rev. D* **24**, 2278 (1981).
- ⁶⁴M. Jarrell and J. E. Gubernatis, *Phys. Rep.* **269**, 133 (1996).
- ⁶⁵D. M. Edwards, *Adv. Phys.* **51**, 1259 (2002).
- ⁶⁶Z. Popović and S. Satpathy, *Phys. Rev. Lett.* **84**, 1603 (2000).
- ⁶⁷T. G. Perring, G. Aepli, Y. Moritomo, and Y. Tokura, *Phys. Rev.*

Lett. **78**, 3197 (1997).

⁶⁸S. Yunoki, J. Hu, A. L. Malvezzi, A. Moreo, N. Furukawa, and E. Dagotto, *Phys. Rev. Lett.* **80**, 845 (1998).

⁶⁹Note that in our calculation we overestimate the critical temperature because we (i) neglect the $t_{2g}-t_{2g}$ superexchange and (ii) because DMFT in general overestimates tendencies towards long-range order. Because of this we performed calculations both in the paramagnetic and ferromagnetic phase, finding a similar resistivity jump at the experimental critical temperature as in experiment. With a properly adjusted $t_{2g}-t_{2g}$ superexchange, we could reproduce the experimental critical temperature without changes in the calculated paramagnetic resistivity in

Fig. 18, and only very minor changes in the ferromagnetic one. However, this would lead to an unphysically large superexchange because of the aforementioned overestimation of critical temperatures in DMFT.

⁷⁰T. A. Maier, M. Jarrell, T. Pruschke, and M. H. Hettler, *Rev. Mod. Phys.* **77**, 1027 (2005).

⁷¹A. A. Katanin, A. Toschi, and K. Held, *Phys. Rev. B* **80**, 075104 (2009).

⁷²A. Toschi, A. A. Katanin, and K. Held, *Phys. Rev. B* **75**, 045118 (2007).

⁷³A. N. Rubtsov, M. I. Katsnelson, and A. I. Lichtenstein, *Phys. Rev. B* **77**, 033101 (2008).